HHS Public Access

Author manuscript

Cancer Immunol Res. Author manuscript; available in PMC 2022 December 03.

Published in final edited form as:

Cancer Immunol Res. 2022 June 03; 10(6): 770–784. doi:10.1158/2326-6066.CIR-21-0559.

Circadian Regulator CLOCK Drives Immunosuppression in Glioblastoma

Wenjing Xuan[1], **Wen-Hao Hsu**[2,3], **Fatima Khan**[1,3], **Madeline Dunterman**[1,3], **Lizhi Pang**[1,3], **Derek A. Wainwright**[1], **Atique U. Ahmed**[1], **Amy B. Heimberger**[1], **Maciej S. Lesniak**[1], **Peiwen Chen**[1,*]

[1]Department of Neurological Surgery, Lou and Jean Malnati Brain Tumor Institute, Robert H Lurie Comprehensive Cancer Center, Feinberg School of Medicine, Northwestern University, Chicago, IL 60611, USA

[2]Department of Cancer Biology, The University of Texas MD Anderson Cancer Center, Houston, Texas 77054, USA

[3]These authors contributed equally to this work.

Abstract

The symbiotic interactions between cancer stem cells and the tumor microenvironment (TME) are critical for tumor progression. However, the molecular mechanism underlying this symbiosis in glioblastoma (GBM) remains enigmatic. Here, we show that circadian locomotor output cycles kaput (CLOCK) and its heterodimeric partner brain and muscle ARNT-like 1 (BMAL1) in glioma stem cells (GSCs) drive immunosuppression in GBM. Integrated analyses of the data from transcriptome profiling, single-cell RNA sequencing, and TCGA datasets, coupled with functional studies, identified legumain (LGMN) as a direct transcriptional target of the CLOCK–BMAL1 complex in GSCs. Moreover, CLOCK-directed olfactomedin-like 3 (OLFML3) upregulates LGMN in GSCs via hypoxia-inducible factor 1-alpha (HIF1α) signaling. Consequently, LGMN promotes microglial infiltration into the GBM TME via upregulating CD162 and polarizes infiltrating microglia towards an immune-suppressive phenotype. In GBM mouse models, inhibition of the CLOCK–OLFML3–HIF1α–LGMN–CD162 axis reduces intratumoral immune-suppressive microglia, increases $CD8^+$ T-cell infiltration, activation and cytotoxicity, and synergizes with anti-PD1 therapy. In human GBM, the CLOCK-regulated LGMN signaling correlates positively with microglial abundance and poor prognosis. Together, these findings uncover the CLOCK–OLFML3–HIF1α–LGMN axis as a molecular switch that controls microglial biology and immunosuppression, thus revealing potential new therapeutic targets for GBM patients.

*Correspondence should be addressed to: Dr. Peiwen Chen (peiwen.chen@northwestern.edu; Tel: 312-503-3822), Department of Neurological Surgery, Feinberg School of Medicine, Northwestern University, Chicago, IL 60611, USA.

Author contributions

W.X., F.K., M.D. and P.C. performed experiments; W.H.H. performed single cell sequencing and TCGA data analysis; L.P. performed flow cytometry data analysis; D.A.W., A.U.A., A.B.H. and M.S.L. contributed to comment this research and manuscript; P.C. conceived the project and wrote the manuscript; and all authors participated in editing the paper.

Conflict of interest: No potential conflicts of interest were disclosed by the authors.

Keywords

Glioblastoma; CLOCK; Microglia; Immunosuppression; HIF1α; LGMN; CD162; Immunotherapy

Introduction

The current standard-of-care for patients with glioblastoma (GBM), a lethal form of primary brain tumor in adults, offers minimal impact on clinical outcomes (1). Genomic profiling of GBM patients has led to the identification of three core signaling pathways, including RTK/RAS/PI3K/PTEN, P53/ARF/MDM2, and RB/CDKN2A, in GBM cells (2,3). These encouraging findings increased the search for targeted therapies; however, almost all efforts to target these core signaling pathways in GBM cells have failed in the clinic (4–7). Increasing evidence shows that signaling from GBM cells not only affects cancer cells, but also regulates the biology of the tumor microenvironment (TME) (8,9). Microglia and bone marrow-derived macrophages (BMDMs, hereafter referred to as macrophages) constitute the most abundant cell population in the GBM TME, and account for up to 50% of the whole tumor mass (10,11). Our prior work has demonstrated that GBM cell signaling can shape a pro-tumor TME by recruiting macrophages (12). Specifically, we found that *PTEN* deletion/mutation in GBM cells upregulates lysyl oxidase to recruit macrophages into the GBM TME, which in turn secrete osteopontin to support glioma cell survival and stimulate angiogenesis (12). These findings highlight symbiotic interactions between GBM cells and the TME and provide a framework from which to identify druggable targets intercepting these co-dependencies in GBM within specific genetic backgrounds.

Circadian rhythm is a conserved phenomenon that plays an important role in regulating cancer cell biology, such as proliferation, metabolism, and DNA repair (13–15). Circadian locomotor output cycles kaput (CLOCK) and its heterodimeric partner brain and muscle ARNT-like 1 (BMAL1, also known as ARNTL) are key transcription factors that can exhibit pro-tumor or anti-tumor effects depending on the TME and cancer types (16,17). The CLOCK–BMAL1 complex has been characterized as oncogenic in GBM, where it can promote glioma cell proliferation and migration (18). We and others have demonstrated that the CLOCK–BMAL1 complex in glioma stem cells (GSCs) not only sustains stemness intrinsically (17,19), but also increases microglial infiltration into the GBM TME in a cell non-autonomous mechanism (17). Nonetheless, the molecular basis by which the CLOCK–BMAL1 complex regulates microglial infiltration is poorly understood. Moreover, whether and how the CLOCK–BMAL1 complex regulates microglia immune-suppressive polarization, modulates T cell–mediated anti-tumor immune response, and affects the responsiveness to immunotherapy are largely unknown.

In this study, we elucidate that legumain (LGMN) is transcriptionally regulated by the CLOCK–BMAL1 complex and upregulated by CLOCK-directed OLFML3–HIF1α axis in mouse and patient-derived GSCs. As a result, LGMN promotes microglial infiltration into the GBM TME via upregulating CD162 (also known as P-selectin ligand) and polarizes infiltrating microglia towards an immune-suppressive phenotype. Inhibition of the CLOCK–HIF1α–LGMN-CD162 axis suppresses GBM growth and synergizes with anti-PD1 therapy

in GBM mouse models. Collectively, our studies decipher the role and mechanism of the CLOCK–BMAL1 complex in regulating a key GBM hallmark of immunosuppression and uncover the CLOCK–OLFML3–HIF1α–LGMN-CD162 axis as an exciting therapeutic target for enhancing immunotherapeutic efficiency in GBM.

Materials and methods

Cell culture

HMC3 microglia; 293T and CT2A cells; and GL261 cells were cultured in Eagle's Minimum Essential Medium (ATCC, # 30-2003), Dulbecco's Modified Eagle's Medium (DMEM; Gibco, #11995-065), and DMEM-Ham's F12 medium (Gibco, #10565-018), respectively, containing 10% FBS (Fisher Scientific, # 16140071) and 1:100 antibiotic-antimycotic (Gibco, #15140-122). For stemness maintenance, CT2A and GL261 cells were cultured in neural stem cell (NSC) proliferation media (Millipore, #SCM005) containing 20 ng/ml epidermal growth factor (EGF; PeproTech, #AF-100-15) and basic fibroblast growth factor (bFGF; PeproTech, #100-18B). These cell lines were purchased from the ATCC, except for GL261 that was obtained from the National Cancer Institute in October 2020. Patient-derived GSCs and mouse QPP7 cells were obtained from Drs. Frederick F Lang and Jian Hu, respectively (The University of Texas MD Anderson Cancer Center, Houston, TX) in October 2020, and were cultured in NSC proliferation media containing 20 ng/ml EGF and bFGF. Early passages of cells were frozen down for future use. Cells were passaged two times per week and were cultured for a maximum of 2 months *in vitro* and underwent four passages for *in vivo* injections. All cells were confirmed to be mycoplasma-free and were maintained at 37 °C and 5% CO_2. Cells were treated with SR9009 (Selleck Chemicals, #S8692, 5 μM), acriflavine (ACF, Sigma, #A8126, 5 μM), LGMN recombinant protein (OriGene, #TP720320, 10–25 ng/ml), RR-11a analog (MedChemExpress, #HY-112205A; 20 nM), PSI-697 (MedChemExpress, #CS-5867; 120 μM) for 24 hrs for conditioned media (CM) collection and protein expression analysis, or 8 hrs for mRNA expression analysis.

Plasmids, viral transfections, and cloning

shRNAs targeting human *CLOCK* and *LGMN*, and mouse *Clock* and *Bmal1* in the pLKO.1 vector (Sigma, #SHC001) were used. Lentiviral particles were generated as we described previously (12). In brief, 8 μg of the shRNA plasmid, 4 μg of the psPAX2 plasmid (Addgene, #12260), and 2 μg of the pMD2.G plasmid (Addgene, #12259) were transfected using Lipofectamine 2000 (Invitrogen, #13778150) into 293T cells plated in 100-mm dishes. Viral supernatant was collected 48 hrs and 72 hrs after transfection and filtered. Cells were infected twice in 48 hrs with viral supernatant containing 10 μg/ml polybrene (Millipore, #TR-1003-G), and then selected using 2 μg/ml puromycin (Millipore, #540411) and tested the expression of CLOCK, LGMN, and BMAL1 by immunoblots. The following mouse and human shRNA sequences (*Clock*: #86:TRCN0000095686 and #74:TRCN0000306474; *Bmal1*: #54:TRCN0000095054 and #57:TRCN0000095057; *LGMN:* #10:TRCN0000029258 and #11:TRCN00000276301) were selected following validation. Doxycycline-inducible plasmid was generated by cloning *CLOCK* shRNA (TRCN0000306475) into a pLKO.1 vector through the Gateway Cloning System (Thermo Fisher, #12535029).

Migration assay

HMC3 microglia were suspended in serum-free culture medium and seeded into 24-well transwell inserts (8.0 μm, Millipore, #MCEP24H48). GSC CM or basal cell culture medium with OLFML3 (OriGene, #TP300923), LGMN (OriGene, #TP720320), or CCL2 (VWR International, #10780-410) recombinant protein (10 ng/ml) was added to the remaining receiver wells. To study the role of LGMN and CD162 in microglial migration, the LGMN inhibitor RR-11a analog (MedChemExpress, #HY-112205A; 20 nM) and P-selectin inhibitor PSI-697 (MedChemExpress, #CS-5867; 120 μM) were used. After 24 hrs, the migrated microglia were fixed and stained with crystal violet (Sigma, #C-3886). The migrated microglia in treatment groups were expressed as a fold change (relative migration) over the control groups.

Immunoblotting

Immunoblotting was performed following the standard protocol (12). Cells were lysed on ice using RIPA buffer (Thermo Scientific, #89901) supplemented with protease inhibitor cocktail (Millipore, #11697498001). Samples were then applied to SDS-PAGE gels (GenScript, #M00652) and blotted onto a nitrocellulose membrane (Bio-Rad, #1704270). Membranes were then incubated with primary antibodies (1:1,000 dilution) overnight at 4 °C. After washing three times, membranes were incubated with HRP-conjugated secondary antibodies (1:1,000 dilution; Cell Signaling, #7076S and #7074S) for 1 hr at room temperature. Signaling was detected by chemiluminescence (Pierce, #34580 and #34076) using the ChemiDoc™ MP Imaging System (Bio-Rad, #17001402). The signal intensity of target proteins was quantified by Image J software (NIH) and normalized against the loading control (e.g., actin or vincullin). Results were expressed as a fold change over the controls. Antibodies used for immunoblotting are listed in Supplementary table 1.

Quantitative real-time PCR (RT-qPCR)

Cells were detached from culture plates with trypsine (Gibco, #25300-054) or Accutase (Millipore, #SCR005), and were pelleted at 1200 rpm for 5 min. RNA was isolated with the RNeasy Mini Kit (Qiagen, #74106), and then reverse-transcribed into cDNA using the All-In-One 5X RT MasterMix (Applied Biological Materials, #G592). RT-qPCR was performed with use of SYBR Green PCR Master Mix (Bio-Rad, #1725275) for distinct genes (e.g., *CLOCK*, *LGMN*, *VEGFA*, *ARG1*, *CD274*, *IFNG*, *IL1B* and *IL10*). Approximately 10 ng of template was used per reaction. The expression of each gene was quantified using the delta-delta CT method and normalized to the housekeeping gene (e.g., *ACTB* or *GAPDH*). Samples (n=3–6 per group) were run on the CFX Connect Real-Time PCR Detection System (Bio-Rad, #1855201).RT-qPCR primers are listed in Supplementary table 2.

Immunohistochemistry and immunofluorescence

Immunohistochemistry and immunofluorescence were performed using a standard protocol as we previously described (12). In brief, a pressure cooker (Bio SB, #7008) was used for antigen retrieval using antigen unmasking solution (Vector Laboratories, #H-3301) at 95 °C for 30 min. After blocking with 10 % goat serum for 1 hr, sections were incubated with primary antibodies (1:200-1:1000 dilution) overnight at 4 °C. For

immunohistochemistry, sections were incubated with rabbit on rodent HRP-polymer (Biocare Medical, Cat# RMR622L) for 40 min and then developed with the Ultravision DAB Plus Substrate Detection System (Thermo Fischer Scientific, #TA-125-QHDX) at room temperature, followed by hematoxylin staining, dehydrated, and coverslipped. For immunofluorescence, sections were washed with PBS and incubated with secondary antibodies (Life Technologies, 1:500) for 1 hr at room temperature in dark, and then were counter-stained with DAPI/anti-fade mounting medium (Vector Laboratories, #H-1200-10). Immunohistochemistry staining in tumor tissue sections were reviewed and scored as previously reported (20,21). Briefly, the staining score = staining intensity × percentage of positive cells. Staining intensity was defined as: 0=negative; 1=weak; 2=moderate; and 3=strong. Percentage of positive cells was assigned as: 0=0%; 1=0–25%; 2=25–50%; 3=50–75%; and 4=75–100%. Antibodies used for immunohistochemistry and immunofluorescence are listed in Supplementary table 1.

ChIP-Seq and ChIP-PCR

GSE134974 (19) containing BMAL1 ChIP-Seq data in GSCs and NSCs was enrolled and the data was analyzed using Integrative Genomics Viewer (Broad Institute). ChIP-PCR was performed using the standard protocol (12). Briefly, chromatin from paraformaldehyde (PFA, Alfa Aesar, #J61899)-fixed GSC272 cells were cross-linked using 1% PFA for 10 min and then reactions were quenched using 0.125 M glycine at room temperature. Cells were lysed with ChIP lysis buffer [10 mM Tris-HCl (pH 8.0), 1 mM EDTA (pH 8.0), 140 mM NaCl, 0.2% SDS, 1% Triton X-100 and 0.1% deoxycholic acid] for 30 min on ice. Chromatin fragmentation was performed using a sonicator, and then solubilized chromatin was incubated with the appropriate mixture of antibody [e.g., anti-CLOCK (Abcam, #ab3517) or anti-BMAL1 (Cell signaling, #14020)] and dynabeads (Thermo Scientific, #A36579) overnight. Immune complexes were then washed with RIPA buffer (Thermo Scientific, #89901), once with RIPA-500 (RIPA with 500 mM NaCl), and once with LiCl wash buffer [10 mM Tris-HCl (pH 8.0), 1 mM EDTA (pH 8.0), 250 mM LiCl, 0.5% NP-40 and 0.5% deoxycholic acid]. Elution and reverse-crosslinking were performed in direct elution buffer [10 mM Tris-Cl (pH 8.0), 5 mM EDTA, 300 mM NaCl, 0.5% SDS] containing proteinase K (Thermo Scientific, #EO0491, 20 mg/ml) at 65 °C overnight. Eluted DNA was purified using AMPure beads (Beckman-Coulter, #A63881), which then was used to perform qPCR. Antibodies used for ChIP-PCR are listed in Supplementary table 1.

Microarray analysis

The GSE140409 (17) containing gene expression data of ishControl and ish*CLOCK* GSC272 cells was enrolled. The differentially expressed genes between two groups were overlapped with the secreted protein database (22) to identify the soluble factors whose expression were reduced by CLOCK depletion. The GSE140409 dataset was used to generate a rank list (ish*CLOCK* versus ishControl) for gene set enrichment analysis (GSEA).

Brain tumor and spleen cell isolation

Mice with neurological deficits or moribund appearance were sacrificed. Brain tumors and spleens were separated and homogenized. Cell suspensions were filtered through 70 μm

strainers (Thermo Fisher, #08-771-2). For brain tumors, myelin and debris were removed by 30/70 Percoll (GE Healthcare, #17-0891-01) gradient separation. The interphase was collected and washed with PBS, and then cells were resuspended for further analysis. For spleen cell isolation, blood cells were lysed using ACK buffer (Thermo Fisher, #A1049201) on ice for 5 min. After deactivation with complete RPMI 1640 media, cell suspensions were centrifuged at 1500 rpm for 10 min at 4°C, and then cells were resuspended in PBS for further analysis.

$CD8^+$ T cell isolation and culture

$CD8^+$ T cells were isolated from the spleens of C57BL/6 mice using a $CD8^+$ T cell isolation kit (Miltenyi Biotec, #130-104-075) following manufacturer's instructions. Then, $CD8^+$ T cells were cultured with RPMI 1640 media (Gibco, #22400-089) containg 10% FBS, 1:100 GlutaMAX (Gibco, #35050061), 50 μM 2-Mercaptoethanol (Sigma, #M7522), 1:100 non-essential amino acids (Gibco, #11140050) and 1:100 antibiotic-antimycotic; and activated with 50 ng/ml recombinant IL2 protein (PeproTech, #212-12) for 72 hrs.

Cytotoxicity assay

The cytotoxicity assay was performed following manufacturer's instructions (Cytotox96 non-radioactive cytotoxicity assay kit, Promega, #G1780). CT2A cells (2×10^4) were used as target cells and co-cultured with IL2-activated $CD8^+$ T cells (1:1, 10:1 and 100:1) for 4 hrs. Before the tumor cell-$CD8^+$ T cell co-incubation, activated $CD8^+$ T cells were co-cultured with HMC3 microglia for 24 hrs. HMC3 microglia were pretreated with GSC272 CM (1:1 dilution with normal culture media) in the presence or absence of LGMN inhibitor RR-11a analog (MedChemExpress, #HY-112205A; 20 nM) for 24 hrs.

Flow cytometry

The single-cell suspensions were incubated with fixable viability dye (Invitrogen, #5211229035) at room temperature for 10 min. After washing with FACS buffer (PBS with 1% BSA), cells were incubated with the indicated antibodies (1:100) and anti-CD16/CD32 cocktail (BioLegend, #103132) for 30 min at room temperature. After staining, cells were washed twice with FACS buffer and then fixed with 1% PFA/FACS buffer at 4°C before performing flow cytometry analysis. Antibodies used for flow cytometry are listed in Supplementary table 1.

Single-cell sequencing data analysis

Single-cell sequencing data of GSE131928 (23) and GSE84465 (24) was used for performing GSC and microglia unsupervised sub-clustering, respectively. CD44, OLIG2 and PDGFRA; and CX3CR1 and GPR34 were selected as the positive control for GSC and microglia clustering, respectively, using principal component analysis with the number of principal components from the elbow point of scree plot. For the differential gene expression of *LGMN* within the microglia sub-cluster, cells were divided into two groups: $LGMN^+$ and $LGMN^-$ groups. DESeq2 v 1.30.0 was performed to obtain the rank list of the differential genes in $LGMN^+$ versus $LGMN^-$ microglia for GSEA.

Computational analysis of human GBM datasets

The TCGA microarray datasets, includingAgilent-4502A (containing 489 GBM patient samples and 10 non-tumor samples) or HG-U133A (containing 528 GBM patient samples and 10 non-tumor samples); or other GBM patient datasets (e.g., the Gravendeel dataset containing 159 GBM patient samples) were enrolled for gene expression, correlation and survival analyses, and gene ontology enrichment analyses (GOEA). The Agilent-4502A TCGA GBM samples were clustered using the 8-gene microglia signature (25) into microglia-high and microglia-low subgroups, using complete-linkage hierarchical clustering.

Mice and intracranial xenograft tumor model

Female C57BL/6 (#0000664) and SCID mice (#ICRSC-F) at 3–4 weeks of age were purchased from the Jackson Laboratory and Taconic Biosciences, respectively. Mice were grouped by 5 animals and maintained under pathogen-free conditions. All animal experiments were performed with the approval of the Institutional Animal Care and Use Committee (IACUC). The intracranial xenograft tumor models were established as we described previously (12). Briefly, mice were anesthetized by intraperitoneal injection of a stock solution containing ketamine (Covetrus, #056344, 100 mg/kg) and xylazine (Akorn, #59399-110-20, 20 mg/kg) and were placed into the stereotactic apparatus (RWD life science, # 68513). A small hole was bored in the skull 1.2 mm anterior and 3.0 mm lateral to the bregma using a dental drill. Cells were injected in a total volume of 5 μL into the right caudate nucleus 3 mm below the surface of the brain using a 10 μL Hamilton syringe with an unbeveled 30-gauge needle. The incision was then stapled closed. Mice were treated with acriflavine (Sigma, #A8126, 5 mg/kg, i.p., daily for 2 weeks), SR9009 (Selleck Chemicals, #S8692, 100 mg/kg, i.p., daily for 2 weeks) or anti-CD162 (Bio X Cell, #BE0186, 10 mg/kg, i.p., every other day for 6 doses) starting at 7 days post-orthotopic tumor cell injection, and/or received the treatment with anti-PD1 (Bio X Cell, #BE0146, 10 mg/kg body weight, i.p., on day 11, 14 and 17). Mice with neurological deficits or moribund appearance were sacrificed. Following the transcardial perfusion with 4% PFA (Alfa Aesar, #J61899), brains were removed and fixed in formalin (Fisher Chemical, #SF100-4), and were processed for paraffin embedded blocks.

Human samples

GBM tissue microarrays (TMAs) containing 35 GBM and 5 normal brain tissues were purchased from US Biomax (#GL806f). These materials were commercially available anonymized and de-identified. According to Northwestern’s Institutional Review Board, the conducted research meets the criteria for exemption #4 (45 CFR 46.101(b) Categories of Exempt Human Subjects Research) and does not constitute human research.

Statistical analysis

Statistical analyses were performed with student *t*-tests for comparison between two groups or with two-way ANOVA test as indicated. Data was represented as mean ± SEM. The survival and correlation analyses in GBM datasets and animal models were performed using the Log-rank (Mantel-Cox) test and the Pearson test, respectively (GraphPad Prism 9). *P*

values were designated as *, $P<0.05$; **, $P<0.01$, and ***, $P<0.001$; n.s., non-significant ($P>0.05$).

Data availability

Microarray dataset (GSE140409), ChIP-Seq dataset (GSE134974), and single-cell RNA sequencing datasets (GSE131928 and GSE84465) were downloaded from the Gene Expression Omnibus. The TCGA datasets and other GBM patient dataset were downloaded from the GlioVis (http://gliovis.bioinfo.cnio.es/).

Results

LGMN promotes microglial migration and is highly expressed in GSCs

At the molecular level, the CLOCK–BMAL1 complex can regulate the expression of nuclear receptors REV-ERBs, which, in turn, form a negative feedback loop to repress BMAL1 (26). As an agonist of nuclear receptors REV-ERBs, SR9009 treatment reduced CLOCK and BMAL1 expression in GSC272 and QPP7 GSCs (Supplementary Fig. S1A–D) and extended the survival of C57BL/6 mice bearing CT2A tumors (17). Consistent with previous studies (27), soft agar colony formation and tumor sphere formation assays demonstrated that CT2A cells possessed a GSC-like phenotype (Supplementary Fig. S1E). To confirm whether SR9009-treated GSCs affect microglial migration, we performed transwell migration assays using the conditioned media (CM) from SR9009-treated and control GSCs. We found that CM from SR9009-treated GSC272 dramatically reduced HMC3 microglial migration (Fig. 1A, B). Flow cytometry revealed that SR9009 treatment significantly reduced the population of $CD45^{low}CD11b^{+}CX3CR1^{+}$ microglia, but did not affect $CD45^{high}CD11b^{+}$ macrophages, in CT2A tumor-bearing brains (Fig. 1C–E). To better understand how the CLOCK–BMAL1 complex triggers microglial infiltration in GBM, we analyzed the microarray profiling data from inducible shRNA control (ishControl) and inducible shRNA *CLOCK* (ish*CLOCK*) knockdown (KD) GSC272 cells (17) and intersected CLOCK-regulated genes with a secreted protein database (22). Consistent with our prior findings (17), we found that *OLFML3*, *POSTN*, *TFPI2*, *LGMN*, and *ALDH9A1* were the top five genes downregulated (KD>75%) by CLOCK depletion (Fig. 1F). Bioinformatics analyses in TCGA GBM dataset demonstrated that the expression of *LGMN, OLFML3*, and *ALDH9A1*, but not of *POSTN* and *TFPI2*, correlated positively with microglial markers CX3CR1, TMEM119 and GPR34 (Supplementary Fig. S1F). GOEA on the Biological Process sub-ontology in TCGA GBM patients demonstrated that *LGMN* and *OLFML3*, but not *ALDH9A1*, correlated positively with leukocyte/myeloid cell migration and chemotaxis (Supplementary Fig. S1G–I). Next, we performed transwell migration assays using recombinant proteins (OLFML3, LGMN, and CCL2) in supplemented media, and found that both LGMN and OLFML3 significantly increased microglial migration showing the activity comparable to that of chemokine CCL2 (Fig. 1G, H). In addition to OLFML3, as we previously reported (17), this study identifies LGMN as a novel CLOCK-regulated chemokine promoting microglial migration. Moreover, by analyzing the microarray profiling data (17), we found that the expression of *LGMN* was higher than that of *OLFML3* in GSC272 (Fig. 1I). To confirm it *in vivo*, we analyzed the single-cell RNA sequencing data from 28 GBM patient tumors (23), and found that *LGMN* expression was higher than that of *OLFML3* in malignant cells (Supplementary Fig. S2A–

C). Within the malignant population (Fig. 1J), we used uniform manifold approximation and projection (UMAP) dimensionality reduction analysis combined with CD44, OLIG2 and PDGFRA as markers to classify GSCs (Supplementary Fig. S2D–F). As a result, we identified three discrete GSC subsets (Fig. 1K) and confirmed that *LGMN* expression was higher than that of *OLFML3* in GSCs from GBM patients (Fig. 1L–N). Notably, the phenotype was reinforced by western blotting showing higher LGMN (the 35 kDa activated isoform) protein relative to OLFML3 in a panel of GSCs, including GSC272, GSC17, TS603, and QPP7 (Fig. 1O, P). Together, these findings suggest that LGMN is a crucial and potent CLOCK-regulated chemokine in GSCs.

CLOCK–BMAL1 complex transcriptionally regulates LGMN in GSCs

To assess whether the CLOCK–BMAL1 complex transcriptionally regulates *LGMN*, we analyzed BMAL1 ChIP-Seq data from human NSCs (e.g., ENSA and hNP1) and GSCs (e.g., T387 and T3565) (19). We found that BMAL1 bound to the *LGMN* promoter in NSCs, which was further increased in GSCs (Fig. 2A, B). ChIP-PCR demonstrated that CLOCK and BMAL1 bound to the *LGMN* promoter in GSC272 cells, and that this binding was reduced upon CLOCK depletion (Fig. 2C). RT-qPCR confirmed that inhibition of the CLOCK–BMAL1 complex by depletion of CLOCK using ish*CLOCK*, or by SR9009 treatment, dramatically reduced the expression of *LGMN* in GSC272 (Fig. 2D, E). Similarly, western blotting demonstrated that shRNA-mediated depletion of CLOCK (Fig. 2F, G) and BMAL1 (Fig. 2H, I), and SR9009 treatment (Fig. 2J, K) significantly reduced the protein abundance of LGMN in QPP7 GSCs and GSC272. Finally, the relationship between LGMN and the CLOCK–BMAL1 complex was reinforced by the positive correlation between LGMN and CLOCK in a panel of GBM patient-derived GSCs, including GSC17, TS603, GSC274 and GSC23 (Fig. 2L, M). Together, these findings suggest that LGMN is transcriptionally regulated by the CLOCK–BMAL1 complex in GSCs.

OLFML3–HIF1α axis upregulates LGMN in GSCs

Together with our prior studies (17), the above findings suggest that both *LGMN* and *OLFML3* are transcriptionally regulated by the CLOCK–BMAL1 complex, but LGMN showed much higher expression, prompting speculation that OLFML3 may upregulate LGMN in GSCs. Using bioinformatics analyses, we found that *LGMN* correlated positively with *OLFML3* in TCGA GBM patients (Fig. 3A). Moreover, western blotting demonstrated that shRNA-mediated depletion of OLFML3 dramatically reduced LGMN expression in GSC272 (Fig. 3B). However, treatment with LGMN inhibitor RR-11a analog did not affect OLFML3 expression in CT2A and GSC272 (Supplementary Fig. S3A, B).

To reveal the molecular basis underlying OLFML3-regulated LGMN expression, we analyzed several datasets with four different comparisons: microarray profiling dataset from GSC272 cells with ish*CLOCK* versus ishControl (17), BMAL1 ChIP-Seq dataset with GSCs versus NSCs (19), as well as TCGA GBM dataset with *OLFML3*-high versus *OLFML3*-low and *BAML1*-high versus *BMAL1*-low. We performed GSEA on hallmark pathways and identified seven overlapping pathways (Fig. 3C). Among them, hypoxia and PI3K/AKT/mTOR pathways are extensively involved in regulating GSC biology. To investigate whether the CLOCK–BMAL1 complex transcriptionally regulates *HIF1A*, we

analyzed BMAL1 ChIP-Seq data (19), and found that BMAL1 bound to the *HIF1A* promoter, and with higher binding activity in GSCs compared to NSCs (Fig. 3D, E). Western blotting demonstrated that inhibition of the CLOCK–BMAL1 complex through shRNA-mediated depletion of CLOCK and BMAL1, or through SR9009 treatment, not only inhibited the expression of OLFML3, as we previously reported (17), but also dramatically reduced HIF1α expression in QPP7 GSCs (Fig. 3F–I) and GSC272 cells (Fig. 3J, K). Moreover, shRNA-mediated depletion of OLFML3 significantly reduced HIF1α expression in GSC272 cells (Fig. 3L, M). Although phospho-p70 S6 Kinase was reduced, inhibition of the CLOCK–BMAL1 complex by ish*CLOCK* did not show any effect on the quantity of AKT and phospho-AKT in GSC272 cells (Supplementary Fig. S3C–E). These findings suggest that HIF1α, but not AKT pathway, is essential for OLFML3-induced LGMN upregulation. Next, we treated GSC272 and CT2A cells with HIF1α inhibitor acriflavine (ACF) and found that such treatment significantly reduced LGMN (Fig. 3N, O), but did not change the expression of OLFML3 (Supplementary Fig. S3F, G). Moreover, LGMN inhibition did not show any effect on HIF1α expression in CT2A and GSC272 cells (Supplementary Fig. S3H, I). We have previously demonstrated that GL261 cells expressed relative high CLOCK expression (17). Tumor sphere formation assay demonstrated that GL261 cells possessed GSC-like phenotype (Supplementary Fig. S3J), consistent with previous work (28). To confirm the importance of the OLFML3-HIF1α-LGMN axis in tumor progression *in vivo*, we treated GL261 tumor-bearing mice with ACF and found that this treatment significantly extended the survival (Fig. 3P). Clinically, the hypoxia signature (from the MSigDB) was upregulated in GBM tumors compared to normal brain tissues (Supplementary Fig. S3K) and correlated positively with poor prognosis in GBM patients (Supplementary Fig. S3L). Collectively, we conclude that OLFML3 upregulates LGMN via HIF1α signaling in GSCs.

LGMN promotes microglial migration via CD162 signaling

To confirm the role of GSC-derived LGMN in microglial migration, we treated GSC272 and CT2A cells with LGMN inhibitor RR-11a analog, and then the CM from treated cells were used to perform transwell migration assays. We found that RR-11a analog treatment in both GSC272 and CT2A cells significantly reduced microglial migration (Fig. 4A–D). Next, we analyzed the single-cell transcriptome data from a cohort of four GBM patients containing both core tumor cells and infiltrating immune cells (24). UMAP dimensionality reduction analysis was used to generate a map of 3589 single cells (Fig. 4E), and CX3CR1 and GPR34 were used as markers to classify microglia (25) (Fig. 4F, G). We found that *LGMN* was highly expressed in microglia in GBM patient tumors (Fig. 4H), suggesting that endogenous LGMN may promote microglial migration. Correspondingly, RR-11a analog treatment in microglia themselves exhibited reduced microglial migration in a dose-dependent manner (Fig. 4I, J).

To understand the potential molecular features underlying LGMN-promoted microglial migration, we generated a rank list showing the differentially expressed genes between $LGMN^{+}$ and $LGMN^{-}$ microglia using the single-cell transcriptome data (Fig. 4K). GSEA focusing on gene ontology pathways demonstrated that leukocyte migration was one of the top pathways enriched in $LGMN^{+}$ microglia (Fig. 4L). Within this signature, 12 genes,

including *CD162*, *APP*, *CD99L2*, *VAV3*, *PPIL2*, *PLCB1*, *VEGFB*, *LGALS3*, *WNK1*, *SELL*, *CYP19A1*, showed an enrichment in *LGMN*$^{+}$ microglia. The further single-cell analysis demonstrated that the expression of *VAV3*, *CD162*, *PLCB1*, *WNK1*, *APP*, *CD99L2*, and *PPIL2* was significantly higher in *LGMN*$^{+}$ microglia compared with these genes in *LGMN*$^{-}$ microglia (Supplementary Fig. S4A). Gene clustering in TCGA GBM patients showed that *CD162*, *SELL*, *CYP19A1*, and *DOK2* exhibited a similar expression pattern with *LGMN* (Supplementary Fig. S4B). Combining these two parameters, we conclude that CD162 is potentially downstream of LGMN signaling, which was further supported by the data from TCGA GBM patients showing that *CD162* correlated positively with *LGMN* (Supplementary Fig. S4C). Consistent with previous studies showing that CD162 is essential for the infiltration of leukocytes, including microglia (29,30), we found that *CD162* correlated positively with microglial markers (e.g., CX3CR1, TMEM119 and GPR34) in TCGA GBM patients (Supplementary Fig. S4D–F). Further investigations using immunoblotting demonstrated that LGMN recombinant protein treatment upregulated the expression of CD162 in HMC3 microglia (Fig. 4M, N), whereas inhibition of this signaling genetically (using *LGMN* shRNAs) and pharmacologically (using LGMN inhibitor RR-11a analog) exhibited an opposite effect (Fig. 4O and Supplementary Fig. S4G–I). Using transwell migration assays, LGMN-supplemented media dramatically increased microglial migration, which was abolished by the treatment with LGMN inhibitor RR-11a analog and P-selectin-CD162 interaction inhibitor PSI-697 (Fig. 4P, Q). Together, these findings suggest that CD162 regulates LGMN-induced microglial migration.

LGMN correlates positively with microglia and is a prognostic factor in GBM patients

To further investigate the role of CLOCK-regulated LGMN in microglial biology, we performed a series of *in silico* analyses on TCGA GBM datasets. GSEA focusing on both hallmark pathways and gene ontology pathways demonstrated that seven out of the top ten pathways enriched in *LGMN*-high GBM patients were associated with immune response (Supplementary Fig. S5A, B). These findings prompted *in silico* immune cell auditing of samples from TCGA GBM patients using 16 types of validated immune cell signatures (12,17,31). This revealed that high *LGMN* expression correlated positively with increased tumor-associated macrophages and microglia (TAMs), microglia and dendritic cells, and to a lesser extent, immature dendritic cells, monocytes, and granulocytes (Supplementary Fig. S5C, D). LGMN expression also correlated with decreased hematopoietic stem cells (Supplementary Fig. S5C). Other immune cell types were not significantly changed (Supplementary Fig. S5C). These studies identified LGMN as an important chemokine for microglia, which was further confirmed by gene clustering data showing that *LGMN* correlated positively with the 8-gene microglial signature (25) in GBM patients (Supplementary Fig. S5E). Using the TCGA GBM dataset, unsupervised clustering with the microglial signature categorized TCGA GBM tumors into two subtypes: microglia-high and microglia-low (Supplementary Fig. S5F), suggesting that a subset of human GBM tumors show prominent infiltration of microglia. Moreover, expression of *LGMN* in the microglia-high samples was higher than those in microglia-low samples (Supplementary Fig. S5G). In addition, the expression of *LGMN* was found to be higher in GBM than that in low-grade glioma (Supplementary Fig. S6A), and higher in grade IV than that in grades II and III patients (Supplementary Fig. S6B). Finally, the survival analysis in the Gravendeel

GBM dataset demonstrated that the expression of *LGMN* correlated negatively with overall survival in GBM patients (Supplementary Fig. S6C). Together, these findings demonstrate that LGMN is a chemokine for microglia that negatively correlates with the survival of GBM patients.

CLOCK–HIF1α–LGMN axis drives microglia polarization towards an immune-suppressive phenotype

Our prior studies have shown that SR9009 treatment significantly extended the survival of C57BL/6 mice implanted with CT2A cells (17). Histological studies further demonstrated that GSC stemness, proliferation, and LGMN expression were dramatically reduced, whereas apoptosis was significantly increased in SR9009-treated CT2A tumors (Supplementary Fig. S7A–D). Moreover, we found that this treatment was accompanied by a significant decrease of intratumoral microglia (Fig. 1C, D), suggesting a potential role of LGMN-regulated microglia in this process. Microglia can be divided into the immune-stimulatory and immune-suppressive phenotypes, which display anti-tumor and pro-tumor effects, respectively (32). We confirmed that GBM-associate microglia are strongly biased towards the immune-suppressive phenotype in tumors from both GSC272 and CT2A models (Fig. 5A, B). Next, we investigated whether the pro-tumor effect of the CLOCK–HIF1α–LGMN axis relates to microglia immune-suppressive polarization in GBM. Flow cytometry demonstrated that GSC272 CM polarized microglia towards an immune-suppressive phenotype, and this effect was abolished when GSC272 cells were pretreated with SR9009 (Fig. 5C, D). Similarly, CM from SR9009-treated CT2A cells downregulated the immune-suppressive microglia markers (e.g., ARG1 and VEGFA) relative to CM from control CT2A cells (Fig. 5E). Consistent with these *in vitro* findings, SR9009 treatment reduced intratumoral $CD45^{low}CD11b^{+}CX3CR1^{+}CD206^{+}$ immune-suppressive microglia in the CT2A model (Fig. 5F, G and Supplementary Fig. S7E). Immunofluorescence staining demonstrated that $CX3CR1^{+}CD206^{+}$ immune-suppressive microglia were significantly reduced in HIF1α inhibitor ACF-treated tumors (Fig. 5H, I). Moreover, RT-qPCR and flow cytometry demonstrated that immune-suppressive microglia were upregulated by LGMN recombinant protein treatment (Fig. 5J), and conversely, downregulated by LGMN inhibitor RR-11a analog treatment in HMC3 microglia (Fig. 5K, L and Supplementary Fig. S7F). Finally, we observed positive expression correlations among CLOCK, HIF1α, and CD206 in human GBM TMAs (protein) (Fig. 5M–O), and positive correlation between *LGMN* and immune-suppressive microglia signature (17) in TCGA GBM dataset (mRNA) (Supplementary Fig. S7G). Together, these *in vitro*, *in vivo* and human GBM findings suggest that the CLOCK–HIF1α–LGMN axis is essential for microglia immune-suppressive polarization.

Inhibition of the CLOCK–OLFML3–HIF1α–LGMN–CD162 axis activates anti-tumor immune response and synergizes with anti-PD1 therapy

Since GBM-associated microglia are immune-suppressive cells and regulated by the CLOCK–HIF1α–LGMN–CD162 axis, we hypothesized that inhibition of this axis can enhance the anti-tumor immune responses to immune checkpoint inhibitors (ICIs). Flow cytometry of spleens from CT2A tumor-bearing mice demonstrated that SR9009 treatment significantly increased $CD3^{+}$ ($CD45^{+}CD3^{+}$), $CD8^{+}$ ($CD45^{+}CD3^{+}CD8^{+}$), and

$CD8^-$ ($CD45^+CD3^+CD8^-$) T cell populations (Fig. 6A, B and Supplementary Fig. S8A). Furthermore, the activated $CD8^+$ T cells ($CD45^+CD3^+CD8^+CD69^+$), but not activated $CD8^-$ T cells ($CD45^+CD3^+CD8^-CD69^+$), were upregulated in the spleens of CT2A tumor-bearing mice upon SR9009 treatment (Fig. 6C and Supplementary Fig. S8B). The enhanced frequency of $CD8^+$ and activated $CD8^+$ T cells was further confirmed by immunofluorescence staining in SR9009-treated CT2A tumors (Fig. 6D, E and Supplementary Fig. S8C, D). Bioinformatics analyses also revealed that activated $CD8^+$ T-cell signature was enriched in *CLOCK*-low patients compared to *CLOCK*-high patients (Fig. 6F). These findings suggest that inhibition of the CLOCK–BMAL1 complex can increase $CD8^+$ T-cell infiltration and activation. Similarly, $CD8^+$ T-cell activation was induced by LGMN inhibition in microglia, as we found that $CD8^+$ T cells expressed significantly more *Ifng* and *Il1b*, and less *Il10* when they were co-cultured with LGMN inhibitor RR-11a analog-treated microglia compared to control microglia (Fig. 6G). Functionally, LGMN inhibition in GSC272 CM-polarized HMC3 microglia promoted $CD8^+$ T cell–mediated CT2A cell cytotoxicity compared to control GSC272 CM-polarized microglia (Fig. 6H). To explore the potential mechanisms underlying this process, we examined the expression of *CD274* (PD-L1, an immune inhibitory molecule), which has been shown as a critical factor that mediates TAM-induced immunosuppression in GBM (33). Investigations on microglia demonstrated that LGMN recombinant protein treatment upregulated PD-L1 expression (Fig. 6I, J), whereas LGMN inhibitor RR-11a analog exhibited an opposite effect (Fig. 6K–M). The TCGA GBM bioinformatics analyses demonstrated that the expression of *CD274* (PD-L1) correlated positively with *CLOCK*, *ARNTL* (BMAL1), *OLFML3*, *HIF1A*, and *LGMN* (Fig. 6N), as well as immune-suppressive microglia signature (Supplementary Fig. S8E). Unsupervised clustering of microglia signature in TCGA GBM patients also demonstrated that expression of *CD274* (PD-L1) in microglia-high tumors was significantly higher than those in microglia-low tumors (Supplementary Fig. S8F). These data prompted an assessment of combined inhibition of the CLOCK–targeted signaling axis and PD1 in GBM-bearing mice. We observed that treatment with SR9009 or anti-CD162 synergized with anti-PD1 therapy to extend survival in the CT2A GBM mouse model (Fig. 6O, P). Together, these findings suggest that inhibition of the CLOCK–OLFML3–HIF1α–LGMN–CD162 axis can enhance $CD8^+$ T-cell infiltration, activation and cytotoxicity, and downregulate PD-L1 expression, and synergize with anti-PD1 therapy to promote meaningful anti-tumor immune responses in GBM-bearing mice.

Discussion

In this study, we uncovered the role and underlying mechanisms of the core circadian regulators CLOCK and BMAL1 in regulating and connecting three GBM hallmarks of stemness, immunosuppression, and hypoxia. We identified LGMN as a key CLOCK-OLFML3–HIF1α axis-regulated factor in GSCs that is essential for microglial infiltration and immune-suppressive polarization. Moreover, we discovered that inhibition of the CLOCK–OLFML3–HIF1α–LMGN–CD162 axis prolongs the survival of GBM-bearing mice and enhances the anti-tumor responsiveness to anti-PD1 therapy. Identification of the pivotal signaling governing the interaction between GSCs (via the CLOCK-OLFML3–

HIF1α–LGMN signaling) and microglia (via the CD162 signaling) illuminates potential therapeutic targets for GBM.

Circadian rhythm regulators have been well-studied in many model organisms (34) and have been linked to tumor progression across cancer types, including lung, breast, and colorectal cancers (35,36). Further evidence demonstrates that the circadian rhythm system is also involved in the pathogenesis of GBM. For example, inhibition of CLOCK and BMAL1 via both genetic and pharmacological approaches has been shown to suppress glioma cell proliferation and migration and inhibit GBM growth (18,37). More recently, we and others have demonstrated that the CLOCK–BMAL1 complex is critical for maintaining GSC stemness and inducing microglial infiltration into the GBM TME (17,19). In the current study, we further extend the molecular understanding for how the CLOCK–BMAL1 complex promotes microglial infiltration and drives immunosuppression in GBM. Moreover, our work highlights the potential of CLOCK-directed microglial biology for enhancing immunotherapy efficiency in GBM patients.

The abundance of infiltrating macrophages and microglia is one of the key hallmarks of GBM (11,32). Infiltrating macrophages have been shown to be the dominant population of myeloid cells contributing to GBM progression (11,12,32,38). However, emerging evidence demonstrates that microglia also play an important role in shaping an immune-suppressive TME and supporting tumor progression in GBM (39,40). The ratio between macrophages and microglia in GBM is dependent on glioma genetic backgrounds and the methods used to quantify them (38). Our prior studies in TCGA GBM patients demonstrated that a microglia, but not macrophage, signature is enriched in CLOCK-high tumors compared to CLOCK-low tumors (17). Along similar lines, our discovery here demonstrates that inhibition of the CLOCK–BMAL1 axis in GBM mouse models reduces microglial infiltration but does not affect macrophage recruitment. Furthermore, we identified a novel CLOCK-regulated chemokine LGMN that plays an essential role in regulating microglial infiltration and microglia-mediated immunosuppression in GBM. These findings are consistent with previous studies showing that circadian components are important for regulating immune response (26,41). Hypoxia is another key hallmark of GBM (42), and we found that inhibition of HIF1α using its inhibitor ACF can prolong the survival of GBM-bearing mice, consistent with previous work (43). Our study also reveals that HIF1α is a critical molecule that mediates the connection between the CLOCK–OLFML3 axis and LGMN signaling in GSCs and regulates CLOCK-directed symbiotic interactions between GSCs and microglia in GBM. These mechanistic findings coupled with the anti-tumor effect of HIF1α inhibitor ACF in GBM mouse models, encourages the development of therapeutic strategies targeting the OLFML3–HIF1α–LGMN axis in CLOCK-high GBM patients.

LGMN is a C13 family of cysteine proteases playing an important role in tumor development, invasion, and metastasis across cancer types (44–46). Our work aligns with previous tumor biology findings that LGMN is highly expressed by both tumor cells (including cancer stem cells) and TAMs (44,47). These findings suggest that as part of the LGMN-directed program of microglial infiltration, microglia themselves could secrete additional LGMN further to increase the infiltration of microglia in a feed-forward manner. In exploring the molecular mechanism underlying LGMN-induced microglial migration, our

unbiased analysis of single-cell transcriptome data from human GBM samples, followed by functional validations, demonstrated that CD162 is a LGMN downstream factor responsible for mediating microglial migration. This role of CD162 is consistent with previous studies showing that CD162 is required for microglial infiltration in a mouse model with neurological disease (30). Once infiltrating into the GBM TME, microglia are usually biased towards an immune-suppressive phenotype. Our work reveals that LGMN functions as a molecular switch controlling microglial immune-suppressive polarization in GBM, which is consistent with previous study highlighting LGMN-regulated TAMs in gastric cancer (48). In addition, it has been demonstrated that inhibition of the CD162–P-selectin axis impairs microglial immune-suppressive polarization in GBM (49). Therefore, it would be useful to reprogram microglia by targeting the LGMN–CD162–P-selectin axis, thus expanding therapeutics for GBM. Together, our study reveals that LGMN not only promotes microglial infiltration into the GBM TME, but also polarizes them towards an immune-suppressive phenotype.

Given their importance in GBM progression, multiple clinical trials are underway for agents targeting TAMs (50). Along similar lines, our mechanistic studies in model systems and correlative studies in human GBMs showing the connection of the CLOCK–OLFML3–HIF1α–LGMN axis and microglial biology (including infiltration and polarization) encourages the design of clinical trials targeting the components of this axis in CLOCK-high GBM patients. Given the immune-suppressive function of microglia, they dampen immune response and activity in the GBM TME (51). It has been well known that GBM patients do not respond to ICIs (e.g., anti-PD1 therapy), which is largely due to the high infiltration of immune-suppressive TAMs and expression of immune inhibitory molecules (52,53). Along these lines, our study highlights that inhibition of the CLOCK–OLFML3–HIF1α–LGMN–CD162 axis impairs microglial infiltration and polarization, enhances $CD8^+$ T-cell infiltration, activation and cytotoxicity, reduces PD-L1 expression, and synergizes with anti-PD1 therapy in GBM-bearing mice. Together, our study encourages the testing of combination regimens inhibiting the CLOCK–BMAL1 complex-mediated microglial biology and immune checkpoints in the treatment of GBM patients.

Supplementary Material

Refer to Web version on PubMed Central for supplementary material.

Acknowledgments

The authors thank Drs. Frederick F Lang and Jian Hu (MD Anderson Cancer Center) for providing patient-derived GSCs and mouse QPP7 cells, and Li Cai (MD Anderson Cancer Center) for the help with gene clustering for microglia.

Financial support:

This work was supported by NIH R00 CA240896, DoD Career Development Award W81XWH-21-1-0380, NIH P50CA221747, Cancer Research Foundation Young Investigator Award, Lynn Sage Scholar Award, American Cancer Society Institutional Research Grant IRG-21-144-27, philanthropic donation from Mindy Jacobson and the Bill Bass Foundation, Northwestern University start-up funds, and the Robert H. Lurie Comprehensive Cancer Center.

References

1. Khosla D Concurrent therapy to enhance radiotherapeutic outcomes in glioblastoma. Ann Transl Med 2016;4(3):54 doi 10.3978/j.issn.2305-5839.2016.01.25. [PubMed: 26904576]
2. Brennan CW, Verhaak RG, McKenna A, Campos B, Noushmehr H, Salama SR, et al. The somatic genomic landscape of glioblastoma. Cell 2013;155(2):462–77 doi 10.1016/j.cell.2013.09.034. [PubMed: 24120142]
3. Cancer Genome Atlas Research N. Comprehensive genomic characterization defines human glioblastoma genes and core pathways. Nature 2008;455(7216):1061–8 doi 10.1038/nature07385. [PubMed: 18772890]
4. Stupp R, Mason WP, van den Bent MJ, Weller M, Fisher B, Taphoorn MJ, et al. Radiotherapy plus concomitant and adjuvant temozolomide for glioblastoma. N Engl J Med 2005;352(10):987–96 doi 10.1056/NEJMoa043330. [PubMed: 15758009]
5. McNamara MG, Lwin Z, Jiang H, Chung C, Millar BA, Sahgal A, et al. Conditional probability of survival and post-progression survival in patients with glioblastoma in the temozolomide treatment era. J Neurooncol 2014;117(1):153–60 doi 10.1007/s11060-014-1368-7. [PubMed: 24469855]
6. Li X, Wu C, Chen N, Gu H, Yen A, Cao L, et al. PI3K/Akt/mTOR signaling pathway and targeted therapy for glioblastoma. Oncotarget 2016;7(22):33440–50 doi 10.18632/oncotarget.7961. [PubMed: 26967052]
7. Westphal M, Maire CL, Lamszus K. EGFR as a Target for Glioblastoma Treatment: An Unfulfilled Promise. Cns Drugs 2017;31(9):723–35 doi 10.1007/s40263-017-0456-6. [PubMed: 28791656]
8. Wang G, Lu X, Dey P, Deng P, Wu CC, Jiang S, et al. Targeting YAP-Dependent MDSC Infiltration Impairs Tumor Progression. Cancer discovery 2016;6(1):80–95 doi 10.1158/2159-8290.CD-15-0224. [PubMed: 26701088]
9. Liao W, Overman MJ, Boutin AT, Shang X, Zhao D, Dey P, et al. KRAS-IRF2 Axis Drives Immune Suppression and Immune Therapy Resistance in Colorectal Cancer. Cancer cell 2019;35(4):559–72 e7 doi 10.1016/j.ccell.2019.02.008. [PubMed: 30905761]
10. Chen Z, Feng X, Herting CJ, Garcia VA, Nie K, Pong WW, et al. Cellular and Molecular Identity of Tumor-Associated Macrophages in Glioblastoma. Cancer Res 2017;77(9):2266–78 doi 10.1158/0008-5472.CAN-16-2310. [PubMed: 28235764]
11. Quail DF, Joyce JA. The Microenvironmental Landscape of Brain Tumors. Cancer Cell 2017;31(3):326–41 doi 10.1016/j.ccell.2017.02.009. [PubMed: 28292436]
12. Chen P, Zhao D, Li J, Liang X, Li J, Chang A, et al. Symbiotic Macrophage-Glioma Cell Interactions Reveal Synthetic Lethality in PTEN-Null Glioma. Cancer Cell 2019;35(6):868–84 e6 doi 10.1016/j.ccell.2019.05.003. [PubMed: 31185211]
13. Masri S, Sassone-Corsi P. The emerging link between cancer, metabolism, and circadian rhythms. Nat Med 2018;24(12):1795–803 doi 10.1038/s41591-018-0271-8. [PubMed: 30523327]
14. Shafi AA, Knudsen KE. Cancer and the Circadian Clock. Cancer Res 2019;79(15):3806–14 doi 10.1158/0008-5472.CAN-19-0566. [PubMed: 31300477]
15. Sulli G, Lam MTY, Panda S. Interplay between Circadian Clock and Cancer: New Frontiers for Cancer Treatment. Trends Cancer 2019;5(8):475–94 doi 10.1016/j.trecan.2019.07.002. [PubMed: 31421905]
16. Shafi AA, Knudsen KE. Cancer and the Circadian Clock. Cancer research 2019 doi 10.1158/0008-5472.CAN-19-0566.
17. Chen P, Hsu WH, Chang A, Tan Z, Lan Z, Zhou A, et al. Circadian Regulator CLOCK Recruits Immune-Suppressive Microglia into the GBM Tumor Microenvironment. Cancer Discov 2020;10(3):371–81 doi 10.1158/2159-8290.CD-19-0400. [PubMed: 31919052]
18. Li A, Lin X, Tan X, Yin B, Han W, Zhao J, et al. Circadian gene Clock contributes to cell proliferation and migration of glioma and is directly regulated by tumor-suppressive miR-124. FEBS Lett 2013;587(15):2455–60 doi 10.1016/j.febslet.2013.06.018. [PubMed: 23792158]
19. Dong Z, Zhang G, Qu M, Gimple RC, Wu Q, Qiu Z, et al. Targeting Glioblastoma Stem Cells through Disruption of the Circadian Clock. Cancer Discov 2019;9(11):1556–73 doi 10.1158/2159-8290.CD-19-0215. [PubMed: 31455674]

20. Chen P, Zuo H, Xiong H, Kolar MJ, Chu Q, Saghatelian A, et al. Gpr132 sensing of lactate mediates tumor-macrophage interplay to promote breast cancer metastasis. Proceedings of the National Academy of Sciences of the United States of America 2017;114(3):580–5 doi 10.1073/pnas.1614035114. [PubMed: 28049847]
21. Su SC, Liu Q, Chen JQ, Chen JN, Chen F, He CH, et al. A Positive Feedback Loop between Mesenchymal-like Cancer Cells and Macrophages Is Essential to Breast Cancer Metastasis. Cancer Cell 2014;25(5):605–20 doi 10.1016/j.ccr.2014.03.021. [PubMed: 24823638]
22. Chen Y, Zhang Y, Yin Y, Gao G, Li S, Jiang Y, et al. SPD--a web-based secreted protein database. Nucleic acids research 2005;33(Database issue):D169–73 doi 10.1093/nar/gki093. [PubMed: 15608170]
23. Neftel C, Laffy J, Filbin MG, Hara T, Shore ME, Rahme GJ, et al. An Integrative Model of Cellular States, Plasticity, and Genetics for Glioblastoma. Cell 2019;178(4):835–49 e21 doi 10.1016/j.cell.2019.06.024. [PubMed: 31327527]
24. Darmanis S, Sloan SA, Croote D, Mignardi M, Chernikova S, Samghababi P, et al. Single-Cell RNA-Seq Analysis of Infiltrating Neoplastic Cells at the Migrating Front of Human Glioblastoma. Cell Rep 2017;21(5):1399–410 doi 10.1016/j.celrep.2017.10.030. [PubMed: 29091775]
25. Ochocka N, Segit P, Walentynowicz KA, Wojnicki K, Cyranowski S, Swatler J, et al. Single-cell RNA sequencing reveals functional heterogeneity of glioma-associated brain macrophages. Nat Commun 2021;12(1):1151 doi 10.1038/s41467-021-21407-w. [PubMed: 33608526]
26. Xuan W, Khan F, James CD, Heimberger AB, Lesniak MS, Chen P. Circadian regulation of cancer cell and tumor microenvironment crosstalk. Trends Cell Biol 2021;31(11):940–50 doi 10.1016/j.tcb.2021.06.008. [PubMed: 34272133]
27. Saha D, Martuza RL, Rabkin SD. Macrophage Polarization Contributes to Glioblastoma Eradication by Combination Immunovirotherapy and Immune Checkpoint Blockade. Cancer Cell 2017;32(2):253–67 e5 doi 10.1016/j.ccell.2017.07.006. [PubMed: 28810147]
28. Wang F, Zhang P, Yang L, Yu X, Ye X, Yang J, et al. Activation of toll-like receptor 2 promotes invasion by upregulating MMPs in glioma stem cells. Am J Transl Res 2015;7(3):607–15. [PubMed: 26045899]
29. Spertini C, Baisse B, Spertini O. Ezrin-radixin-moesin-binding sequence of PSGL-1 glycoprotein regulates leukocyte rolling on selectins and activation of extracellular signal-regulated kinases. J Biol Chem 2012;287(13):10693–702 doi 10.1074/jbc.M111.318022. [PubMed: 22311979]
30. Kronenberg G, Uhlemann R, Richter N, Klempin F, Wegner S, Staerck L, et al. Distinguishing features of microglia- and monocyte-derived macrophages after stroke. Acta Neuropathol 2018;135(4):551–68 doi 10.1007/s00401-017-1795-6. [PubMed: 29249001]
31. Masuda T, Sankowski R, Staszewski O, Bottcher C, Amann L, Sagar, et al. Spatial and temporal heterogeneity of mouse and human microglia at single-cell resolution. Nature 2019;566(7744):388–92 doi 10.1038/s41586-019-0924-x. [PubMed: 30760929]
32. Hambardzumyan D, Gutmann DH, Kettenmann H. The role of microglia and macrophages in glioma maintenance and progression. Nat Neurosci 2016;19(1):20–7 doi 10.1038/nn.4185. [PubMed: 26713745]
33. Bloch O, Crane CA, Kaur R, Safaee M, Rutkowski MJ, Parsa AT. Gliomas promote immunosuppression through induction of B7-H1 expression in tumor-associated macrophages. Clin Cancer Res 2013;19(12):3165–75 doi 10.1158/1078-0432.CCR-12-3314. [PubMed: 23613317]
34. Kronauer RE, Gunzelmann G, Van Dongen HPA, Doyle FJ, Klerman EB. Uncovering physiologic mechanisms of circadian rhythms and sleep/wake regulation through mathematical modeling. J Biol Rhythm 2007;22(3):233–45 doi 10.1177/0748730407301237.
35. Schernhammer ES, Laden F, Speizer FE, Willett WC, Hunter DJ, Kawachi I, et al. Night-shift work and risk of colorectal cancer in the nurses' health study. Journal of the National Cancer Institute 2003;95(11):825–8. [PubMed: 12783938]
36. Fu L, Kettner NM. The circadian clock in cancer development and therapy. Prog Mol Biol Transl Sci 2013;119:221–82 doi 10.1016/B978-0-12-396971-2.00009-9. [PubMed: 23899600]

37. Sulli G, Rommel A, Wang XJ, Kolar MJ, Puca F, Saghatelian A, et al. Pharmacological activation of REV-ERBs is lethal in cancer and oncogene-induced senescence. Nature 2018;553(7688):351-+ doi 10.1038/nature25170. [PubMed: 29320480]
38. Xuan W, Lesniak MS, James CD, Heimberger AB, Chen P. Context-Dependent Glioblastoma-Macrophage/Microglia Symbiosis and Associated Mechanisms. Trends Immunol 2021;42(4):280–92 doi 10.1016/j.it.2021.02.004. [PubMed: 33663953]
39. Matias D, Predes D, Niemeyer Filho P, Lopes MC, Abreu JG, Lima FRS, et al. Microglia-glioblastoma interactions: New role for Wnt signaling. Biochim Biophys Acta Rev Cancer 2017;1868(1):333–40 doi 10.1016/j.bbcan.2017.05.007. [PubMed: 28554667]
40. Dumas AA, Pomella N, Rosser G, Guglielmi L, Vinel C, Millner TO, et al. Microglia promote glioblastoma via mTOR-mediated immunosuppression of the tumour microenvironment. EMBO J 2020;39(15):e103790 doi 10.15252/embj.2019103790. [PubMed: 32567735]
41. Scheiermann C, Kunisaki Y, Frenette PS. Circadian control of the immune system. Nat Rev Immunol 2013;13(3):190–8 doi 10.1038/nri3386. [PubMed: 23391992]
42. Hambardzumyan D, Bergers G. Glioblastoma: Defining Tumor Niches. Trends Cancer 2015;1(4):252–65 doi 10.1016/j.trecan.2015.10.009. [PubMed: 27088132]
43. Mangraviti A, Raghavan T, Volpin F, Skuli N, Gullotti D, Zhou J, et al. HIF-1alpha- Targeting Acriflavine Provides Long Term Survival and Radiological Tumor Response in Brain Cancer Therapy. Sci Rep 2017;7(1):14978 doi 10.1038/s41598-017-14990-w. [PubMed: 29097800]
44. Liu Z, Xiong M, Gong JB, Zhang Y, Bai N, Luo YP, et al. Legumain protease-activated TAT-liposome cargo for targeting tumours and their microenvironment. Nat Commun 2014;5 doi ARTN 4280 10.1038/ncomms5280.
45. Zhen Y, Chunlei G, Wenzhi S, Shuangtao Z, Na L, Rongrong W, et al. Clinicopathologic significance of legumain overexpression in cancer: a systematic review and meta-analysis. Sci Rep 2015;5:16599 doi 10.1038/srep16599. [PubMed: 26607955]
46. Qi Q, Obianyo O, Du Y, Fu H, Li S, Ye K. Blockade of Asparagine Endopeptidase Inhibits Cancer Metastasis. J Med Chem 2017;60(17):7244–55 doi 10.1021/acs.jmedchem.7b00228. [PubMed: 28820254]
47. Liu C, Sun CZ, Huang HN, Janda K, Edgington T. Overexpression of legumain in tumors is significant for invasion/metastasis and a candidate enzymatic target for prodrug therapy. Cancer Res 2003;63(11):2957–64. [PubMed: 12782603]
48. Wang H, Chen B, Lin Y, Zhou Y, Li X. Legumain Promotes Gastric Cancer Progression Through Tumor-associated Macrophages In vitro and In vivo. Int J Biol Sci 2020;16(1):172–80 doi 10.7150/ijbs.36467. [PubMed: 31892854]
49. Yeini E, Ofek P, Pozzi S, Albeck N, Ben-Shushan D, Tiram G, et al. P-selectin axis plays a key role in microglia immunophenotype and glioblastoma progression. Nat Commun 2021;12(1):1912 doi 10.1038/s41467-021-22186-0. [PubMed: 33771989]
50. Wei J, Chen P, Gupta P, Ott M, Zamler D, Kassab C, et al. Immune biology of glioma-associated macrophages and microglia: functional and therapeutic implications. Neuro Oncol 2020;22(2):180–94 doi 10.1093/neuonc/noz212. [PubMed: 31679017]
51. See AP, Parker JJ, Waziri A. The role of regulatory T cells and microglia in glioblastoma-associated immunosuppression. J Neurooncol 2015;123(3):405–12 doi 10.1007/s11060-015-1849-3. [PubMed: 26123363]
52. Geraldo LHM, Garcia C, da Fonseca ACC, Dubois LGF, de Sampaio ESTCL, Matias D, et al. Glioblastoma Therapy in the Age of Molecular Medicine. Trends in cancer 2019;5(1):46–65 doi 10.1016/j.trecan.2018.11.002. [PubMed: 30616755]
53. Lamano JB, Lamano JB, Li YD, DiDomenico JD, Choy W, Veliceasa D, et al. Glioblastoma-Derived IL6 Induces Immunosuppressive Peripheral Myeloid Cell PD-L1 and Promotes Tumor Growth. Clinical cancer research : an official journal of the American Association for Cancer Research 2019;25(12):3643–57 doi 10.1158/1078-0432.CCR-18-2402. [PubMed: 30824583]

Synopsis

The minimal responsiveness of glioblastoma to immunotherapy is largely due to robust infiltration of immune-suppressive microglia. Inhibition of the CLOCK–OLFML3–HIF1α–LGMN axis reduces microglial infiltration and immune-suppressive polarization, increases anti-tumor immunity, and enhances immunotherapy efficiency.

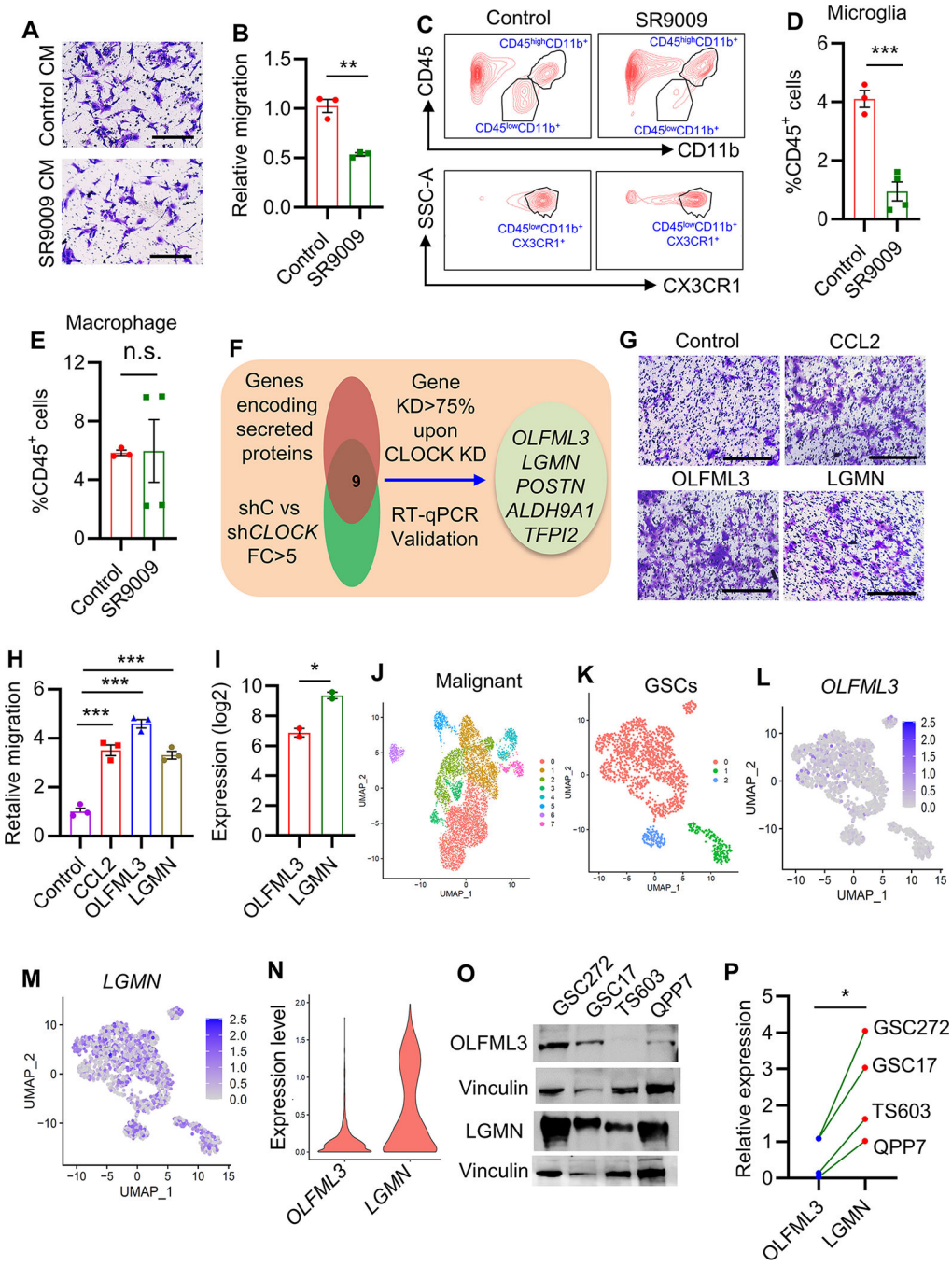

Fig. 1. LGMN is a potent microglia chemokine and highly expressed in GSCs.

(**A, B**) Representative images (**A**) and quantification (**B**) of transwell migration analysis for HMC3 microglia after stimulation with conditional medium (CM) from GSC272 cells pre-treated with or without SR9009 (5 μM) for 24 hrs. Scale bar, 200 μm. n=3 biological replicates. ** $P<0.01$.

(**C-E**) Representative (**C**) and quantification of flow cytometry analysis for the percentage of $CD45^{low}CD11b^{+}CX3CR1^{+}$ microglia (**D**) and $CD45^{high}CD11b^{+}$ macrophages (**E**) in size

matched tumor-bearing brains of CT2A modes treated with or without SR9009 (100 mg/kg, i.p., daily). n=3–4 biological replicates. ***P<0.001; n.s., not significant.

(**F**) Identification of five genes (*OLFML3*, *POSTN*, *TFPI2*, *LGMN*, and *ALDH9A1*) that encode secreted proteins and are downregulated by *CLOCK* knockdown in GSCs.

(**G, H**) Representative images (**G**) and quantification (**H**) of transwell migration analysis for HMC3 microglia after stimulation with recombinant CCL2, OLFML3 or LGMN protein (10 ng/ml). Scale bar, 50 μm. CCL2 was used as a positive control. n=3 biological replicates. ***P<0.001.

(**I**) The mRNA expression of *LGMN* and *OLFML3* in GSC272 cells based on microarray data analysis. n=2 biological replicates. *P<0.05.

(**J**) High-resolution uniform manifold approximation and projection (UMAP) dimensional reduction of malignant cells from brain tumor samples of a cohort of 28 GBM patients.

(**K**) UMAP dimensional reduction of glioma stem cells (GSCs) on the basis of the expression pattern of GSC markers (including CD44, PDGFRA and OLIG2); GSCs were partitioned into three distinct clusters.

(**L, M**) Pattern representing single-cell gene expression of *OLFML3* (**L**) and *LGMN* (**M**) in GSCs. Intensity of the blue color indicates the expression of individual cells.

(**N**) Violin plot showing the expression of *OLFML3* and *LGMN* in GSCs based on single-cell RNA sequencing data from GBM patient tumor samples.

(**O, P**) Representative (**O**) and quantification (**P**) of immunoblots for OLFML3 and LGMN in cell lysates of GSC272, GSC17, TS603, and QPP7 GSCs. *P<0.05.

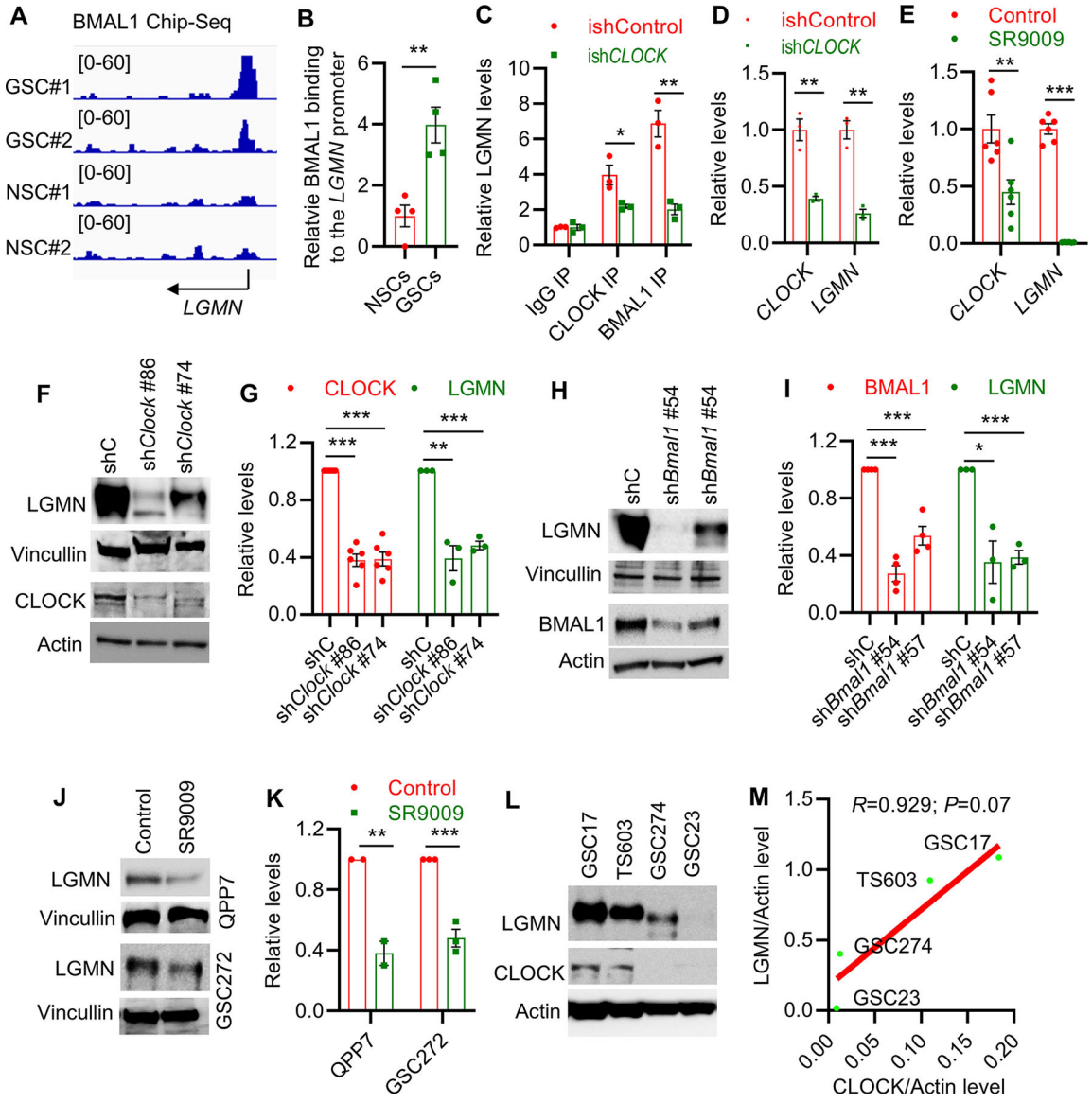

Fig. 2. CLOCK–BMAL1 complex transcriptionally regulates LGMN in GSCs.

(**A, B**) ChIP-seq data analysis (**A**) and quantification (**B**) of BMAL1-enriched profiles at the *LGMN* promotor in GSC #1 and #2 (T387 and T3565), and NSC #1 and #2 (ENSA and hNP1). n=4 biological replicates. *** $P<0.01$.

(**C**) Quantification of ChIP-PCR shows that CLOCK and BMAL1 can directly bind to the *LGMN* promoter in ishControl and ish*CLOCK* GSC272 cells. n=3 biological replicates. * $P<0.05$; ** $P<0.01$.

(**D**) RT-qPCR shows the expression of *CLOCK* and *LGMN* in ishControl and ish*CLOCK* GSC272 cells. n=3 biological replicates. ** $P<0.01$.

(**E**) RT-qPCR shows the expression of *CLOCK* and *LGMN* in Control and SR9009 (5 μM)-treated GSC272 cells. n=6 biological replicates. ** $P<0.01$; *** $P<0.001$.

(**F, G**) Representative (**F**) and quantification (**G**) of immunoblots for LGMN and CLOCK in cell lysates of QPP7 GSCs expressing shRNA control (shC) and *Clock* shRNAs. n=3–6 biological replicates. ** $P<0.01$; *** $P<0.001$.

(**H, I**) Representative (**H**) and quantification (**I**) of immunoblots for LGMN and BAML1 in cell lysates of QPP7 GSCs expressing shRNA control (shC) and *Bmal1* (*Arntl*) shRNAs. n=3–4 biological replicates. * $P<0.05$; *** $P<0.001$.

(**J, K**) Representative (**J**) and quantification (**K**) of immunoblots for LGMN in cell lysates of QPP7 GSCs and GSC272 treated with or without SR9009 (5 μM). n=3 biological replicates. ** $P<0.01$; *** $P<0.001$.

(**L, M**) Representative immunoblots (**L**) and correlation analysis (**M**) of LGMN and CLOCK (the expression was normalized against Actin) in cell lysates of GSC17, TS603, GSC274, and GSC23. R and P values are shown.

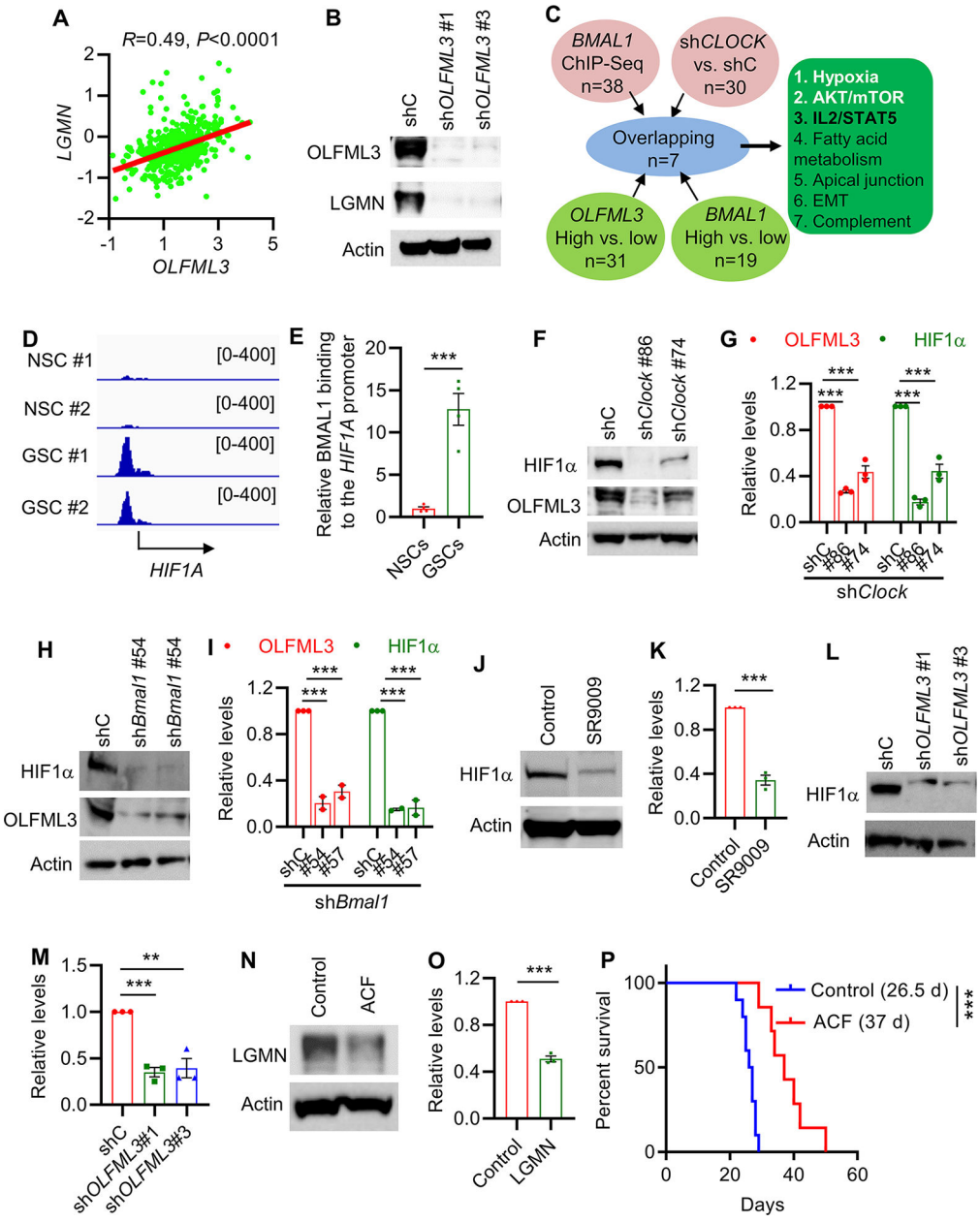

Fig. 3. OLFML3–HIF1α axis upregulates LGMN in GSCs.

(**A**) Correlation of *LGMN* and *OLFML3* in TCGA GBM patients. *R* and *P* values are shown.

(**B**) Immunoblots for OLFML3 and LGMN in cell lysates of GSC272 cells expressing shRNA control (shC) and *OLFML3* shRNAs.

(**C**) Identification of seven overlapping hallmark pathways (as indicated) in different datasets with four comparisons (BMAL1 ChIP-Seq data: GSCs versus NSCs; GSC272 microarray data: sh*CLOCK* vs shControl; TCGA GBM dataset: *OLFML3*-high versus *OLFML3*-low and *BMAL1*-high versus *BMAL1*-low).

(**D, E**) ChIP-seq data analysis (**D**) and quantification (**E**) of BMAL1-enriched profiles at the *HIF1A* promotor in GSC #1 and #2 (T387 and T3565), and NSC #1 and #2 (ENSA and hNP1). n=4 biological replicates. *** *P*<0.001.

(**F, G**) Representative (**F**) and quantification (**G**) of immunoblots for OLFML3 and HIF1α in cell lysates of QPP7 GSCs expressing shRNA control (shC) and *Clock* shRNAs. n=3 biological replicates. *** $P<0.001$.

(**H, I**) Representative (**H**) and quantification (**I**) of immunoblots for OLFML3 and HIF1α in cell lysates of QPP7 GSCs expressing shRNA control (shC) and *Bmal1* shRNAs. n=2–3 biological replicates. *** $P<0.001$.

(**J, K**) Representative (**J**) and quantification (**K**) of immunoblots for HIF1α in cell lysates of GSC272 cells treated with or without SR9009 (5 μM). n=3 biological replicates. *** $P<0.001$.

(**L, M**) Representative (**L**) and quantification (**M**) of immunoblots for HIF1α in cell lysates of GSC272 cells expressing shRNA control (shC) and *OLFML3* shRNAs. n=3 biological replicates. ** $P<0.01$; *** $P<0.001$.

(**N, O**) Representative (**N**) and quantification (**O**) of immunoblots for LGMN in cell lysates of GSC272 cells treated with or without HIF1α inhibitor ACF (5 μM). n=3 biological replicates. *** $P<0.001$.

(**P**) Survival curves of C57BL/6 mice implanted with GL261 cells (2×10^4 cells/mouse). Mice were treated with HIF1α inhibitor ACF (5 mg/kg body weight, i.p., daily) starting at 7 d post-orthotopic injection of GL261 cells. n=6 or 10 mice/group. ***$P<0.001$.

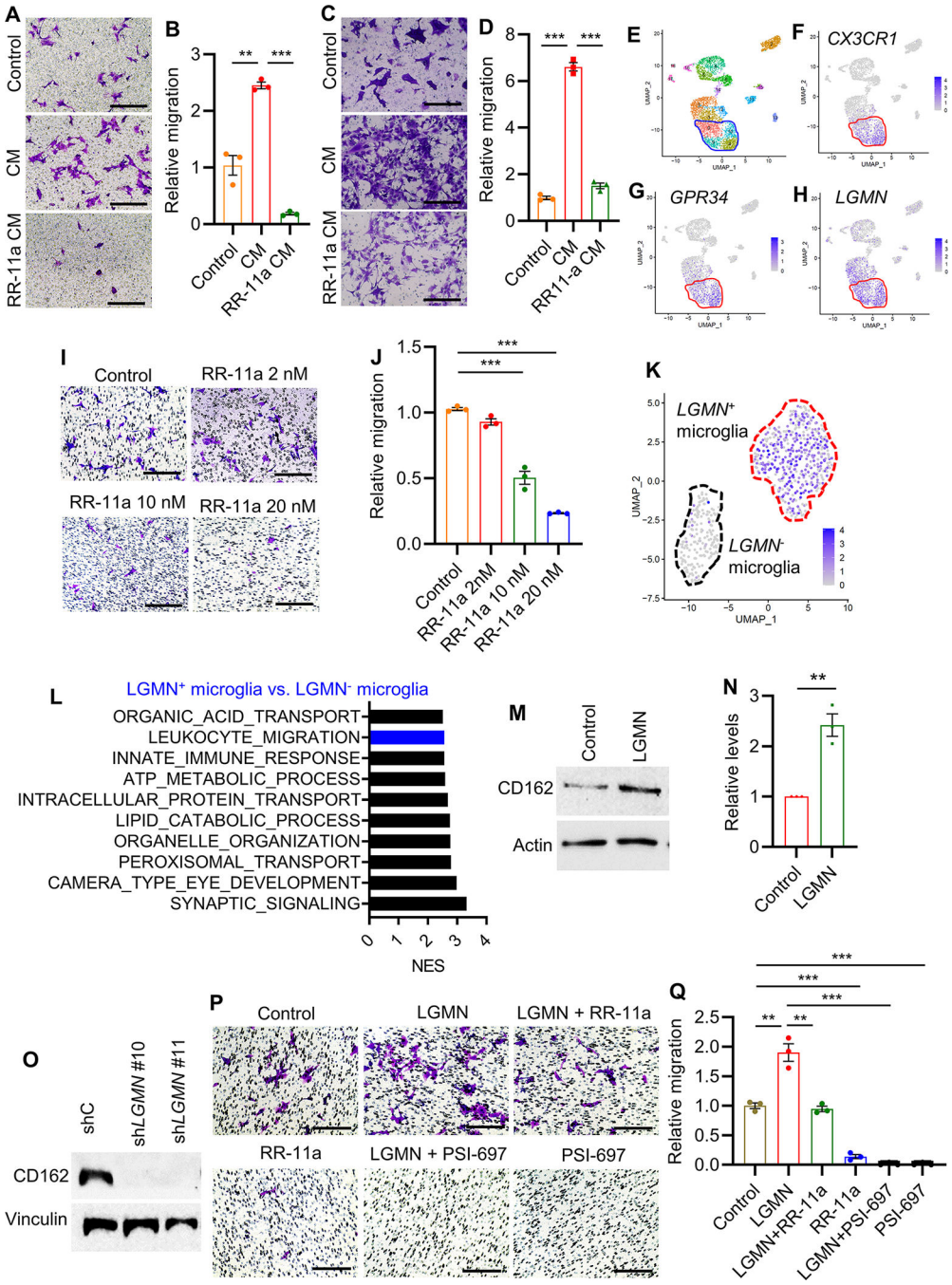

Fig. 4. LGMN promotes microglial migration via the CD162 signaling.

(**A, B**) Representative images (**A**) and quantification (**B**) of transwell migration analysis for HMC3 microglia after stimulation with conditional medium (CM) from GSC272 cells pre-treated with or without LGMN inhibitor RR-11a analog (20 nM) for 24 hrs. Scale bar, 200 μm. n=3 biological replicates. ***P*<0.01, ****P*<0.001.

(**C, D**) Representative images (**C**) and quantification (**D**) of transwell migration analysis for HMC3 microglia after stimulation with CM from CT2A cells pre-treated with or

without RR-11a analog (20 nM) for 24 hrs. Scale bar, 200 μm. n=3 biological replicates. *** P<0.001.

(**E**) UMAP dimensional reduction of single cells (n=3,589) from brain tumor samples of a cohort of 4 GBM patients

(**F, G**) UMAP dimensional reduction of microglia (as highlighted) on the basis of *CX3CR1* (**F**) and *GPR34* (**G**) expression pattern.

(**H**) Gene expression pattern representing single-cell gene expression of *LGMN* in microglia (as highlighted). Intensity of the blue color indicates the expression of individual cells.

(**I, J**) Representative images (**I**) and quantification (**J**) of transwell migration analysis for HMC3 microglia after treatment with RR-11a analog at indicated concentrations. Scale bar, 200 μm. n=3 biological replicates. *** P<0.001.

(**K**) UMAP dimensional reduction of microglia from single cell sequencing data of a cohort of four GBM patient tumors, and microglia were partitioned into two distinct clusters: $LGMN^+$ and $LGMN^-$ microglia.

(**L**) GSEA analysis on GBM patient single cell data shows the top 10 enriched gene ontology pathways in $LGMN^+$ microglia compared with $LGMN^-$ microglia. Blue highlighted pathway relates to leukocyte migration.

(**M, N**) Representative (**M**) and quantification (**N**) of immunoblots for CD162 in cell lysates of HMC3 microglia treated with or without LGMN (10 ng/ml). n=3 biological replicates. ** P<0.01.

(**O**) Immunoblots for CD162 in cell lysates of HMC3 microglia expressing shRNA control (shC) and *LGMN* shRNAs.

(**P, Q**) Representative images (**P**) and quantification (**Q**) of transwell migration analysis for HMC3 microglia after stimulation with recombinant LGMN protein (10 ng/ml) in the presence or absence of LGMN inhibitor RR-11a analog (20 nM), or p-selectin inhibitor PSI-697 (120 μM). Scale bar, 200 μm. n=3 biological replicates. ** P<0.01, *** P<0.001.

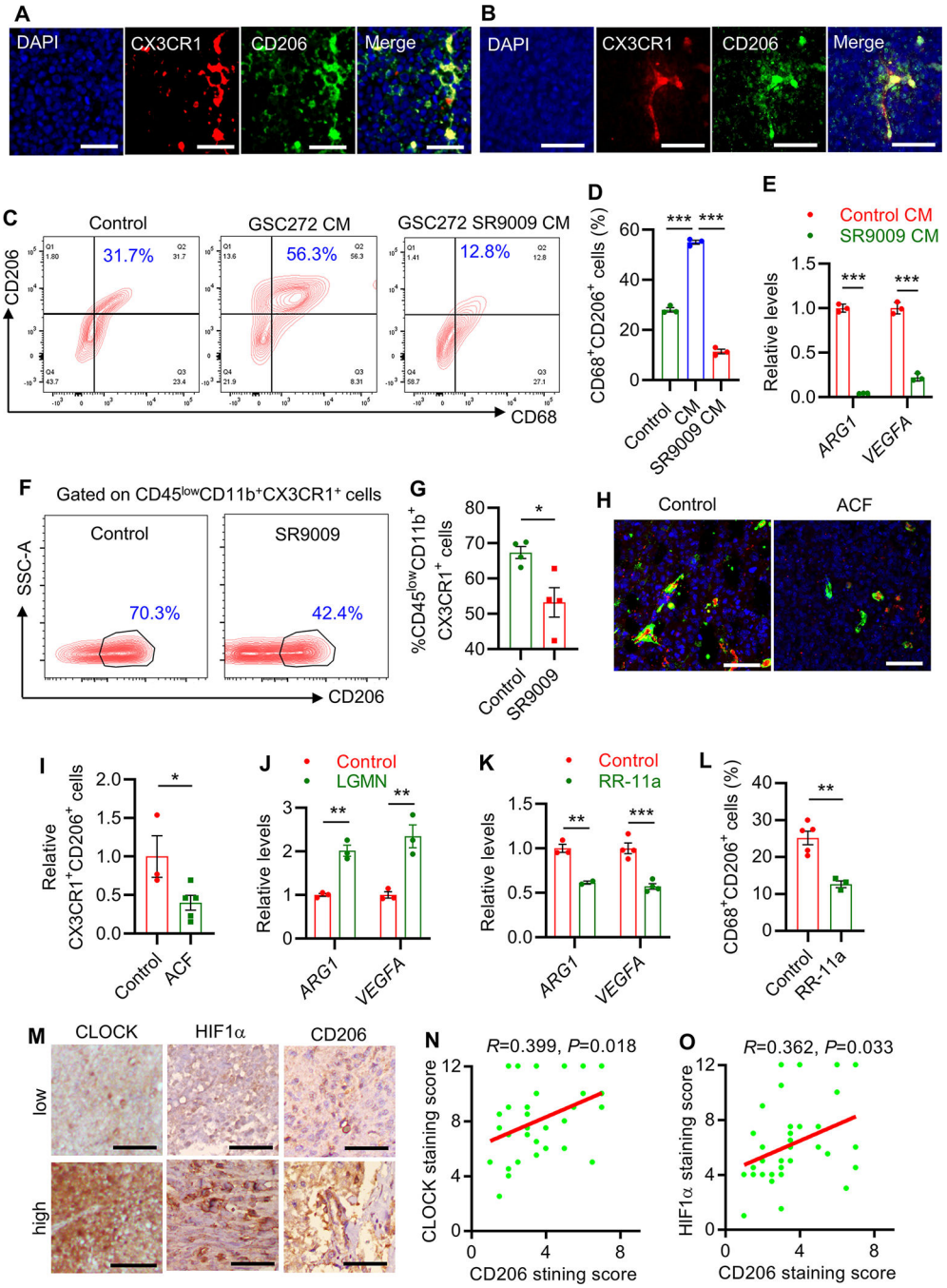

Figure 5. CLOCK–HIF1α–LGMN axis drives microglia polarization towards an immune-suppressive phenotype

(**A, B**) Co-immunofluorescence staining for CX3CR1 (red) and CD206 (green) in GBM tumors from GSC272 (**A**) and CT2A (**B**) models implanted in SCID and C57BL/6, respectively. Scale bar, 50 μm.

(**C, D**) Representative (**C**) and quantification (**D**) of flow cytometry for the percentage of $CD68^{+}CD206^{+}$ cells in HMC3 microglia treated with or without conditioned media (CM)

from control GSC272 cells and SR9009-treated GSC272 cells. n=3 biological replicates; *** P <0.001.

(**E**) RT-qPCR shows the expression of *ARG1* and *VEGFA* in HMC3 microglia treated with CM from control and SR9009-treated CT2A cells. n=3 biological replicates; *** P<0.001.

(**F, G**) Representative (**F**) and quantification (**G**) of flow cytometry for intratumoral $CD45^{low}CD11b^{+}CX3CR1^{+}CD206^{+}$ immune-suppressive microglia in size matched tumors from CT2A model treated with or without SR9009 (100 mg/kg, i.p., daily). The percentage of $CD45^{+}CD11b^{+}CX3CR1^{+}CD206^{+}$ microglia out of $CD45^{+}CD11b^{+}CX3CR1^{+}$ microglia is shown. n=4 biological replicates; * P<0.05.

(**H, I**) Representative (**H**) and quantification (**I**) of immunofluorescence for CX3CR1 (green) and CD206 (red) in mouse tumors from Control and HIF1α inhibitor ACF-treated GL261 models. Scale bar, 75 μm; n=3 biological replicates; * P <0.05.

(**J**) RT-qPCR shows the expression of immune-suppressive microglia markers (including ARG1 and VEGFA) in Control and LGMN recombinant protein (25 ng/ml)-treated HMC3 cells. n=3 biological replicates; ** P<0.01.

(**K**) RT-qPCR shows the expression of *ARG1* and *VEGFA* in Control and LGMN inhibitor RR-11a analog (20 nM) treated HMC3 cells. n=3–4 biological replicates; ** P<0.01, *** P<0.001.

(**L**) Quantification of flow cytometry for the percentage of $CD68^{+}CD206^{+}$ cells in HMC3 microglia treated with or without LGMN inhibitor RR-11a analog (20 nM). n=3–5 biological replicates; ** P <0.01.

(**M**-**O**) CLOCK and HIF1α expression is positively correlated with immune-suppressive microglia marker CD206 in human GBM TMA samples. Representative images (**M**) showing low and high expression of CLOCK, HIF1α, and CD206 in human GBM TMAs (n = 35). Scale bar, 50 μm; Quantification data showing strong positive correlations between CLOCK and CD206 (**N**), or HIF1α and CD206 (**O**) in human GBM TMAs. R and P values are shown.

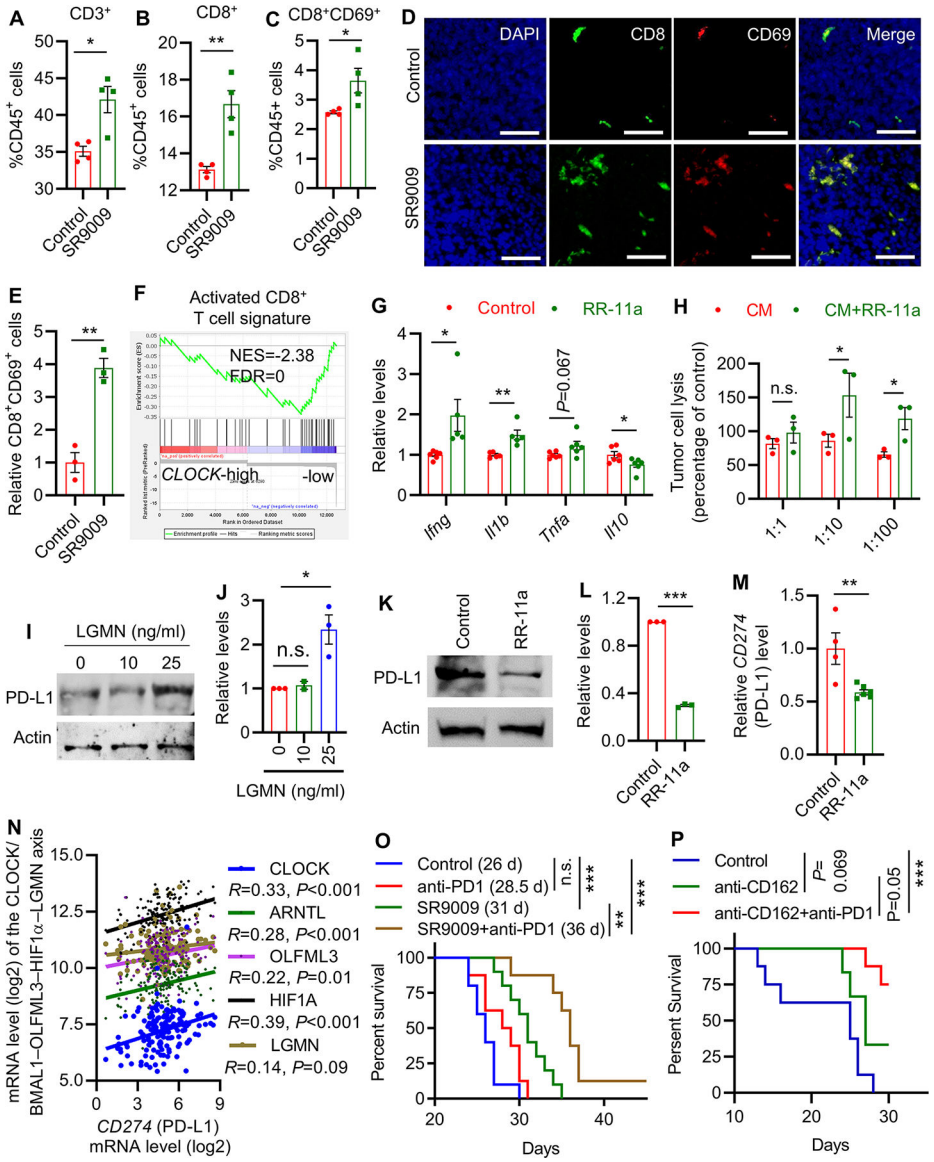

Figure 6. Inhibition of the CLOCK–OLFML3–HIF1α–LGMN–CD162 axis activates anti-tumor immune response and synergizes with anti-PD1 therapy.

(**A-C**) Percentage of $CD3^+$ (**A**), $CD3^+CD8^+$ (**B**), and activated $CD8^+$ ($CD3^+CD8^+CD69^+$; **C**) T cells in the spleens of CT2A tumor-bearing mice treatment with or without SR9009 (100 mg/kg, i.p., daily). n=4 biological replicates. **P*<0.05; ***P*<0.01.

(**D, E**) Representative images (**D**) and quantification (**E**) of immunofluorescence for CD8 and CD69 in CT2A tumors treated with or without SR9009. Mice were treated with SR9009 (100 mg/kg, i.p., daily) for 10 days starting at day 7 post-orthotopic injection (2×10^4 cells). Scale bar, 50 μm. n=3 biological replicates. ***P*<0.01.

(**F**) GSEA for activated $CD8^+$ T-cell signature in *CLOCK*-high patients compared to *CLOCK*-low patients from TCGA GBM dataset.

(**G**) RT-qPCR shows the expression of *Ifng*, *Il1b*, *Tnfa*, and *Il10* in IL2-activated $CD8^+$ T cells when they were co-cultured with microglia (1:1 ratio) for 24 hrs. Microglia were

pre-treated with or without LGMN inhibitor RR-11a analog (20 nM) for 24 hrs. n=5–6 biological replicates; * P<0.05, ** P<0.01.

(**H**) CT2A tumor cell cytotoxicity induced by IL2-activated $CD8^+$ T cells co-cultured with GSC272 CM-treated HMC3 microglia in the presence or absence of LGMN inhibitor RR-11a analog (20 nM). Data was expressed as the percentage of cytotoxicity induced by IL2-activated $CD8^+$ T cells (without co-culture of microglia). n = 3 biological replicates; *P< 0.05 (two-way ANOVA test).

(**I, J**) Representative (**I**) and quantification (**J**) of immunoblots for PD-L1 in cell lysates of HMC3 microglia treated with LGMN recombinant protein at indicated concentrations for 24 hrs. n=3 biological replicates; * P<0.05; n.s., not significant.

(**K, L**) Representative (**K**) and quantification (**L**) of immunoblots for PD-L1 in cell lysates of HMC3 microglia treated with LGMN inhibitor RR-11a analog (20 nM) for 24 hrs. n=3 biological replicates; *** P<0.001.

(**M**) RT-qPCR shows the expression of CD274 (PD-L1) in HMC3 microglia treated with or without LGMN inhibitor RR-11a analog (20 nM) for 16 hrs. n=4–6 biological replicates; ** P<0.01.

(**N**) Correlation of *CD274* (PD-L1) and the CLOCK–OLFML3–HIF1α–LGMN axis in TCGA GBM patients (RNA-Seq platform). R and P values are shown.

(**O**) Survival curves of C57BL/6 mice implanted with CT2A cells (2×10^4 cells/mouse). Mice were treated with SR9009 (100 mg/kg, i.p., daily) on day 7, and then received the treatment with IgG or anti-PD1 (10 mg/kg body weight, i.p.) on day 11, 14 and 17. n=8–10 mice for each group. n.s., not significant; ** P < 0.01, *** P < 0.001.

(**P**) Survival curves of C57BL/6 mice implanted with CT2A cells (2×10^4 cells/mouse). Mice were treated with anti-CD162 on day 8 (10 mg/kg, i.p., every other day for 6 doses), and received the treatment with anti-PD1 (10 mg/kg body weight, i.p.) on day 11, 14 and 17. n=6–8 mice for each group. *** P < 0.001.